Microdeposition of metal and oxide structures using ultrashort laser pulses

Article *in* Applied Physics A · April 1998

Impact Factor: 1.7 · DOI: 10.1007/s003390050717

7 authors, including:

Ioanna Zergioti
National Technical University of Athens
136 PUBLICATIONS **1,716** CITATIONS
SEE PROFILE

Sakellaris Mailis
University of Southampton
184 PUBLICATIONS **1,372** CITATIONS
SEE PROFILE

Pagona Papakonstantinou
Ulster University
138 PUBLICATIONS **3,670** CITATIONS
SEE PROFILE

Rapid Microwave Synthesis of CO Tolerant Reduced Graphene Oxide-Supported Platinum Electrocatalysts for Oxidation of Methanol

Surbhi Sharma,[†,⊥] Abhijit Ganguly,[†,⊥] Pagona Papakonstantinou,*[,†] Xiaopei Miao,[‡] Meixian Li,[‡] John L. Hutchison,[§] Michael Delichatsios,[∥] and Sebastian Ukleja[∥]

Nanotechnology and Advanced Materials Research Institute, NAMRI, University of Ulster, Jordanstown campus, BT37 0QB UK, Institute of Analytical Chemistry, Peking University, Beijing, 100871 P.R. China, Department of Materials, University of Oxford, Parks Road, OX1 3PH UK, and Fire Safety Engineering Research and Technology Centre, University of Ulster, Jordanstown campus, BT37 0QB UK

Received: August 19, 2010; Revised Manuscript Received: September 25, 2010

Reduced graphene oxide/platinum supported electrocatalysts (Pt/RGO) were synthesized by employing a fast and eco-friendly microwave-assisted polyol process, which facilitated the simultaneous reduction of graphene oxide and formation of Pt nanocrystals. This system was tested for potential use as an anode material through the electrooxidation of methanol. Compared to the commercial carbon-supported Pt electrocatalysts, the Pt/RGO showed an unprecedented CO poisoning tolerance, high electrochemical active surface area, and high catalytic mass activity for methanol oxidation reaction, demonstrated by increases of 110, 134, and 60%, respectively. We found that the high concentration of oxygen functional groups on reduced graphene oxide plays a major role on the removal of carbonaceous species on the adjacent Pt sites, underlining a synergetic effect between the oxygen moieties on graphene support and Pt nanoparticles. The present microwave assisted synthesis of Pt/RGO provides a new path to prepare electrocatalysts with excellent electrocatalytic activity and CO tolerance, which is of great significance in energy-related applications.

Introduction

The controlled assembly of different nanoscale materials, having distinct chemical or physical properties into novel hybrid nanostructures with unique functionality, constitutes a key challenge in nanoscience.[1−4] Hybrid nanostructures if appropriately designed are expected to combine the merits of the individual building nanomaterials. In particular, the coupling of nanostructured forms of carbon with metal catalysts presents unique opportunities to fabricate novel hybrid electrode structures for use in electrocatalytic applications such as biosensing and energy conversion devices.[3−5]

Fuel cells convert chemical energy directly into electrical energy by catalytic conversion of a fuel, such as hydrogen or methanol, with high efficiency and low emission of pollutants.[3,4,6−9] Despite their advantages, a few technological barriers remain to be overcome before successful commercial applications can be achieved. One such barrier is the CO poisoning of the platinum (Pt) electrode material, whereby CO occupies active sites on the Pt catalyst and prevents fuel oxidation. CO poisoning is especially problematic for direct methanol fuel cells (DMFCs) because CO is always present in critical amounts as an intermediate in methanol oxidation. A major strategy for considerably attenuating CO poisoning is to alloy Pt with other oxophilic elements such as Ru, Ni, Pd, and Au.[10−16] Two main mechanisms have been proposed to explain this improved tolerance to CO. Within the bifunctional mechanism model,[10−12,16] adsorbed OH species generated by water dissociation at the platinum/ruthenium edge promote the oxidation of CO (the promotion effect). According to the intrinsic or ligand mechanism, ruthenium modifies the electronic structure of neighboring Pt atoms, reducing their affinity for CO.[15,16] Although these additional elements reduce catalyst poisoning to a certain extent, their incorporation makes the DMFC less cost efficient. Thus, more competent and cost-effective options still need to be investigated.

A key component that contributes to the high electrocatalytic activity is the nature of the carbon support, which can assist both in dispersing the metal catalyst and in facilitating electron transport, as well as in promoting mass transfer kinetics at the electrode surface. The oxidation of the carbon supports, prior to the catalyst deposition, was found to increase the electrode activity for methanol oxidation.[12,17,18] The presence of surface oxides modifies the chemical and physical properties of the carbon, improving wettability and accessibility of methanol to the electroactive surface. In addition, the oxygen functional groups act as nucleation centers or anchoring sites, limiting the particle growth, improving the dispersion of metallic crystallites, and enhancing the stability of the supported catalysts. At present, there is a lack of understanding on the role of oxygen groups on the CO tolerance, and this issue has rarely been investigated. Moreover, heavily oxidized supports have been avoided because of their low electrical conductivity.

Graphene, a single sheet of graphite, is an especially promising form of nanoscale carbon with a rare combination of extremely high specific surface area, exceptional thermal/electrical conductivity, and good chemical and thermal stability. The utilization of graphene as a two-dimensional support to anchor catalyst nanoparticles (NPs) and facilitate electron transport opens up new possibilities for designing the next generation catalysts.[19,20] Current mass-scale production of graphene is based on chemical exfoliation of graphite in strong acids. The oxidation procedure introduces oxygen atoms to the

* Corresponding author. E-mail: p.papakonstantinou@ulster.ac.uk.
[†] University of Ulster.
[‡] Peking University.
[§] University of Oxford.
[∥] University of Ulster.
[⊥] These authors contributed equally to this work.

10.1021/jp107872z
Published on Web 10/20/2010

TABLE 1: Synthesis Conditions and Final Pt Loading for the Samples

conditions/ samples	starting concentration of precursor, M	duration of microwave, s	final loading (From TGA) %
Pt/RGO1	0.05	50	30.08
Pt/RGO2	0.05	100	47.37
Pt/RGO3	0.1	50	67.29
Pt/C			21.63

basal planes and edges of graphene layers in the form of functional groups, such as hydroxyl, epoxide, keto, and carboxyl. The resulting graphene oxide (GO) is highly resistive and has to be converted to a conductor by reduction, using heat treatment and/or toxic reducing agents to restore the sp^2 hybrid network.[5,21,22]

This work focuses on two important aspects of reduced GO (RGO) systems. (1) Demonstration of one-step environmentally friendly microwave-assisted polyol process (MWAPP) for the synthesis of the electrocatalytic RGO-supported Pt nanocrystals.[11,17] (2) Elucidation of the important role of the residual oxygen groups of the RGO support on the removal of carbonaceous species. In this one-pot synthesis method, ethylene glycol (EG) serves as both dispersing and reductive agent for both metal ions and GO, facilitating the formation of Pt nanocrystals on RGO. The use of microwaves serves to accelerate the reductive processes and has advantages compared to other heating methods in terms of energy efficiency, speed, uniformity, and implementation simplicity. To gain an understanding of the role of oxide centers on the support, we investigated their influence on the methanol oxidation reaction (MOR) at the well characterized Pt/RGO electrodes. We show that the constructed hybrids present catalytic activity, stability, and tolerance to poison effect for MOR, outperforming the commercial carbon-supported Pt electrocatalysts (Pt/C). To best of our knowledge, such excellent antipoisoning performance has rarely been observed on Pt−carbon-based supports. The results strongly indicate that the presence of residual oxygen groups on RGO plays a vital role on antipoisoning activity of Pt/RGO electrocatalysts.

Experimental Section

Synthesis. Starting material GO was prepared from natural graphite powder by using a modified Hummer's oxidation process.[21] For Pt/RGO hybrids synthesis, GO (40 mg) was suspended in EG (20 mL) and ultrasonicated for 60 min. The appropriate amount of aqueous solution of potassium hexachloroplatinate (K_2PtCl_6, 0.05−0.1 M) was added to the suspension, and the solution was stirred. The exact amounts of K_2PtCl_6 for each sample are reported in Table 1. Subsequently, the pH was appropriately adjusted to a value of 8 by adding a KOH/EG solution (0.4M) dropwise. After ultrasonication for 60 min, the yellow/brown polyol mixture was put into a microwave oven (700 W) for the desired duration (50−100 s, see Table S1 in the Suporting Information). The black precipitate obtained was washed several times by using acetone and collected after drying at 50 °C overnight in vacuum. All chemicals were purchased from Sigma. A commercially available Pt reference catalyst (Pt/C), Pt-loaded carbon black with 21.6 wt % Pt, was purchased from Alfa Aesar.

Characterization. Transmission electron microscopy (TEM) imaging and analysis were performed on a JEOL 4000EX equipped with a LaB6 electron gun operated at 400 kV. X-ray photoemission spectroscopy (XPS) was carried out by using a high-resolution SCIENTA ECSA 300 equipped with monochromatic Al Kα ($h\nu = 1486.6$ eV) X-ray source at Daresbury Laboratory. XPS measurements were also performed in house by using a Kratos Axis Ultra DLD spectrometer equipped with monochromatic Al Kα ($h\nu = 1486.6$ eV). X-ray diffraction (XRD) studies were performed on a Bruker D8-Discover diffractometer fitted with a Gobel Mirror (CuKα radiation source $\lambda = 1.540$ Å). Diffraction scans of thin films were recorded for 2θ values between 5 and 90° with a step size of 0.04° and a dwell time of 10 s per increment. Thermo gravimetric analysis (TGA) was performed in Oxygen (N_2 50 mL min^{-1} and O_2 50 mL min^{-1}) by using Mettler Toledo TGA (model TGA/SDTA851e) at a heating rate of 5 °C min^{-1} up to 1000 °C.

Electrochemical Measurements. Cyclic voltammetry (CV) and chrono-amperometry (CA) measurements were performed with an AUTOLAB PGSTAT 20 potentiostat at room temperature. A conventional three-electrode cell was used with Ag/AgCl (saturated KCl) electrode, platinum wire, and a glassy carbon electrode (GCE, diameter: 3 mm) as reference, counter and working electrodes, respectively. Before each experiment, the GCE was polished by using 0.3 and 0.05 μm alumina powders followed by washing in ethanol and distilled water. Then, 20 μL aqueous solution of Pt/RGO hybrids (0.5 mg/mL) or Pt/C was dropped on the GCE surface and dried under an infrared lamp.

Results and Discussion

Synthesis of Pt/RGO Hybrids. Here, we used GO as a starting material, prepared from graphite powder by using modified Hummer's oxidation process.[21] The principle of the assemblage of Pt NPs on RGO via one-pot chemical procedure (MWAPP process) is outlined in Figure 1a (details in Experimental Section). GO was mixed ultrasonically with metal precursor K_2PtCl_6 in EG, after which the polyol solution was rapidly heated in a microwave oven to decompose EG, yielding in situ generated reducing species. This resulted in simultaneous reduction of Pt precursor and GO. The produced fine metal particles perceived potential nucleation centers at the support material suspended in the solution, thus resulting in the synthesis of metallic NPs supported on the reduced GO. Microwave exposure transformed the starting yellow/brown colored solution into a black solution, indicating the reduction of GO. The reduction of GO was confirmed from both XPS and XRD analysis. The enhancement of the carbon/oxygen ratio (from 2.08 to 2.86), estimated from XPS analysis, has provided a quantitative measure of the GO reduction.[21] By varying the amount of K_2PtCl_6 and the irradiation time, the Pt loadings were controlled from 30 to 67 wt % (estimated from TGA, Figure S1, Supporting Information). The catalysts thus obtained are denoted as Pt/RGO1, Pt/RGO2, and Pt/RGO3, with a measured carbon/oxygen ratio of 2.37 (26.79 at% of oxygen), 2.75 (23.48 at %), and 2.86 (21.78 at. %) and metal loading of 30.1, 47.4, and 67.3 wt %, respectively (Tables 1 and 2).

Structural Characterisations. The as-synthesized GO has an oxygen content of 32.5 at% (a measured carbon/oxygen ratio of 2.08, Table 2). The composition is in good agreement with values reported for similar oxidation processes.[21] Because a variety of oxygen functional groups (O-moieties) are attached on the edge planes as well as on either side of the basal planes, well dispersed nanoclusters on the surface of the reduced graphene sheets are envisaged. Such anticipation was confirmed by high-resolution TEM (HRTEM) observations (Figure 1b, Figure S3 in the Supporting Information). It is worth mentioning that these Pt NPs anchored onto the RGO surface can also prevent $\pi-\pi$ stacking between the layers and create functional separation between individual sheets.

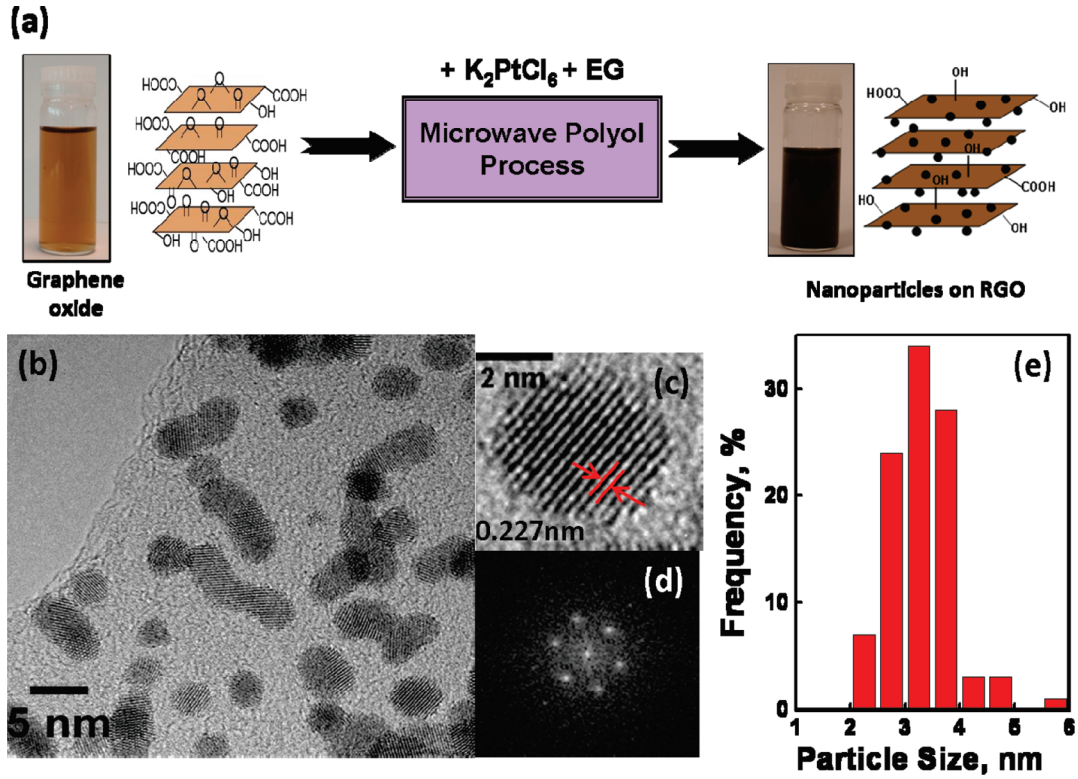

Figure 1. (a) Scheme of MWAPP synthesis of Pt/RGO hybrids. (b) TEM image of Pt/RGO1. (c) HRTEM image and (d) FFTs of a single Pt NP (fcc structures of Pt (111) with lattice angle = 63.44°, a = 3.92 Å, and d-spacing = 0.226 nm). (f) Pt NPs size distribution on Pt/RGO1.

TABLE 2: XPS Analysis: Elemental Atomic Concentrations of As-Prepared Samples

	atomic concentration % (mass conc%)			
element/sample	Pt	O	C	C:O
Pt/RGO1	9.53 (60.91) ± 0.5	26.79 (14.04) ± 0.3	63.68 (25.05) ± 0.7	2.37
Pt/RGO2	11.88 (66.79) ± 0.4	23.48 (10.83) ± 1.2	64.64 (22.38) ± 0.8	2.75
Pt/RGO3	15.78 (73.71) ± 0.2	21.78 (8.34) ± 1.5	62.43 (17.95) ± 1.7	2.86
Pt/C	02.24 (26.78) ± 0.2	04.46 (4.38) ± 0.6	93.31 (68.84) ± 0.4	20.92
GO		32.46 (38.58) ± 0.7	67.54 (61.42) ± 0.5	2.08

TEM Studies. Figure 1b shows a TEM image of Pt/RGO1 (30.1% Pt) revealing that the Pt nanocrystals are distributed quite uniformly on the surface of the sheet (for TEM image of GO, see Figure S2 in the Supporting Information). The high-resolution images showing Pt lattice fringes and fast fourier transforms (FFTs) of single Pt NP (Figure 1c,d, respectively) revealed fcc structures for Pt (111). Uniform distribution of Pt NPs on the RGO support is facilitated by the widespread presence of oxygen groups on RGO. TEM studies performed on Pt/RGO2 and Pt/RGO3 (Figure S3 in the Supporting Information) also showed uniform particle distribution for the Pt NPs. As expected because of the increased loading, a denser NP distribution was observed for Pt/RGO3. It can also be seen that, with the increased loading, the particle size distribution has become broader. The average particle size was determined to be 3.31 ± 0.06 nm for Pt/RGO1, 4.89 ± 0.67 nm for Pt/RGO2, and 5.81 ± 0.90 nm for Pt/RGO3 (Figure S3 in the Supporting Information). The results were consistent with the XRD evaluations.

XRD Analysis. Figure 2 shows XRD patterns of GO and Pt/RGOs, together with that of a commercial Pt reference catalyst Pt/C (Pt-loaded carbon black, 21.6 wt% Pt), for comparison purposes. The complete oxidation of GO was evidenced by the appearance of a new broad (002) peak (GO peak) at 2θ = 11.2° with 0.78 nm d-spacing, in place of the characteristic C(002) graphite peak (2θ = 26.4°, 3.34 Å d-spacing). The increased d-spacing of GO sheets is due to the presence of abundant O-moieties on both sides of the graphene sheet causing an atomic-scale roughness on the graphene sheet.

Upon the formation of Pt/RGO1, the GO peak reduced in intensity and moved to the slightly higher diffraction angle of 11.6°, whereas the C (002) graphite peak shifted to a smaller value of 23.44°. The concurrent presence of both peaks indicates that the graphitic layers of the hybrids are not completely reduced. As the Pt loading increased to 47.4 and 67.3 wt%, by doubling the microwave treatment time (Pt/RGO2) and concentration of Pt precursor (Pt/RGO3), respectively, the GO peak was completely suppressed. The suppression of the GO peak indicated that the conjugated graphene network (sp^2 carbon) has been re-established because of the reduction process. Simulta-

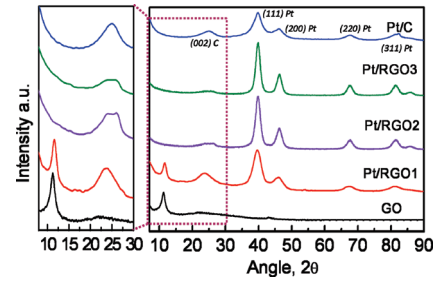

Figure 2. XRD spectra for GO, Pt/RGO hybrids, and Pt/C.

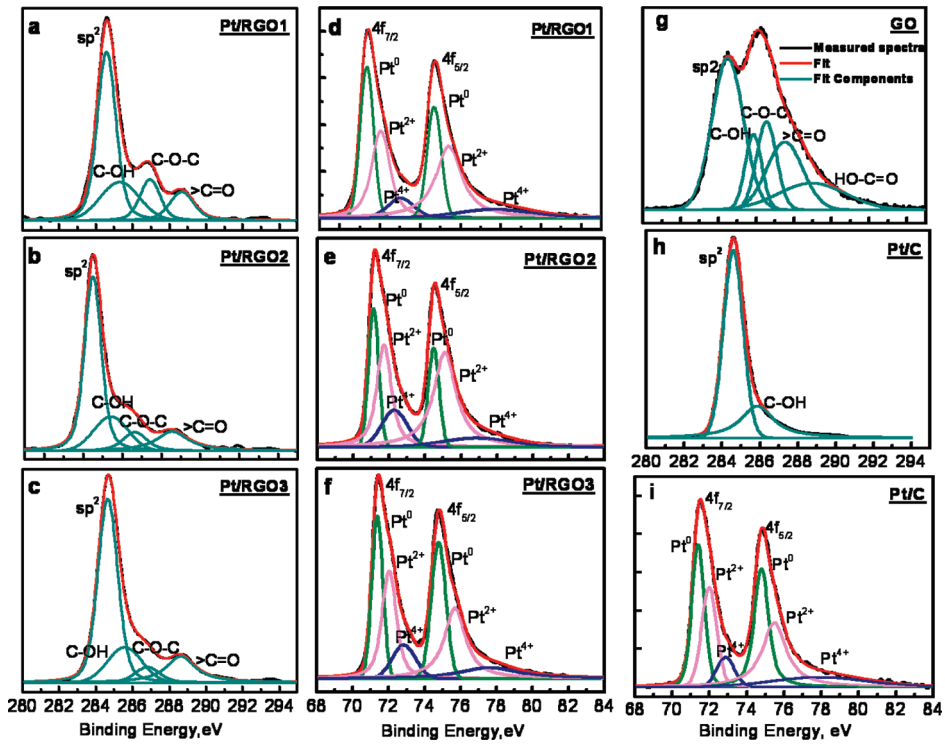

Figure 3. High-resolution deconvoluted XPS spectra: (a−c) C1s for Pt/RGO hybrids; (d−f) corresponding Pt 4f; (g) C1s for GO; (h) C1s for Pt/C; and (i) corresponding Pt 4f.

neously, the carbon (002) peak became broader with a FWHM of 4.94 and 4.72° for Pt/RGO2 and Pt/RGO3, respectively, indicating the presence of a range of oxidation states.

The diffraction peaks at 2θ = 39.5, 46.2, 67.1°, and 81.2° are attributed to the (111), (200), (220), and (311) crystalline planes of the fcc structure of Pt, respectively, and provide evidence for the crystallinity of the formed Pt NPs. Another observation is that Pt/RGO2 appears to have a much sharper Pt (111) peak which may make one think that it has the highest Pt loading. However, XRD analysis was performed on the samples in thin-film configuration (prepared by drop-drying on Si substrates), and the film thickness and uniformity (surface topography) may vary from sample to sample. Hence, the absolute intensity of the Pt XRD peak cannot define the actual amount of loading. The high intensity of the Pt peaks for Pt/RGO2 could be due to slightly thicker (therefore, more Pt was available for detection) sample giving rise to higher counts. For quantitative analysis of Pt loading, we performed TGA measurements.

Pt NP sizes were determined to be 3.2, 4.8, and 5.1 nm for Pt/RGO1, Pt/RGO2, and Pt/RGO3, respectively; the values are consistent with TEM results. For the Pt/C, the characteristic peaks for fcc Pt nanocrystals (39.84, 46.08, 68.04, and 82.32°) and C (24.96°) were observed. The particle size was found to be 3.5 nm.

XPS Analysis. Figure 3 presents the C 1s and Pt 4f XPS spectra of Pt/RGO and Pt/C together with GO, for comparison purposes (for O 1s spectra, see Figure S4 in the Supporting Information). The peak assignments and the corresponding relative contributions, estimated from the curve fitting of the spectra, are displayed in Table S1 (Supporting Information). The C1s band of GO material exhibited the presence of two maxima separated by 1.72 eV, which is a characteristic of heavily oxidized graphite (Figure 3g). Peak fitting of this band yielded five components, located at 284.5 (FWHM = 1.96 eV), 285.9 (FWHM =1.03 eV), 286.6 (FWHM = 1.25 eV), 287.5 (FWHM = 2.25 eV), and 289.0 eV (FWHM = 4.17 eV) corresponding to C═C/C−C in aromatic rings, C−OH (hydroxyl), C−O−C (epoxy, ether), >C═O (carbonyl, ketone), and OH−C═O (carboxylic) groups, respectively, as illustrated in Table S1 in the Supporting Information.

XPS analysis further confirmed the reduction of GO through loss of oxygen moieties and the formation of new sp^2 C−C bonds as evidenced by the loss of the double peak and the significant increase in C/O ratio in Pt/RGO via the microwave-assisted polyol reduction. In the Pt/RGO hybrids, the intensity of the C═C/C−C peak increased, along with a dramatic decrease of the overlapping peaks at 285.5−289.0 eV (Figure 3a−c and Table S1 in the Supporting Information). Although the MWPP reduction substantially reduced the O-moieties in comparison to the starting GO, they were still observable on the Pt/RGO hybrids. In contrast, Pt/C showed only a small presence of hydroxyl group (Figure 3h).

Pt 4f spectra of all samples showed the expected doublets for Pt $4f^{7/2}$ and Pt $4f^{5/2}$, with Pt^0, Pt^{2+}, and Pt^{4+} oxidation states (Figure 3d−f,i). It is interesting to note that, in spite of significant amounts of oxygen present in GO, a respectable percentage of Pt remained in its native state (Pt^0) in Pt/RGOs (Figure 3, Table S1 in the Supporting Information). The hybrids Pt/RGO1 and Pt/RGO3 exhibited 38 and 40% of Pt^0, respectively, close to Pt/C (43%, Table S1 in the Supporting Information). However, Pt/RGO2 was found to have the lowest Pt^0 content (28%); probably, the longer exposure to microwaves led to the oxidation of Pt once the nucleation process of Pt NPs was complete.

XPS is a surface analysis technique with a probe depth of only 10 nm, and hence, it cannot estimate the total bulk metal loading of the prepared samples that had a thickness of a few micrometers. Moreover, XPS analysis was performed on samples in thin-film configuration (prepared by drop-drying on Si substrates), and therefore, the film thickness and uniformity (surface topography) may vary from sample to sample. For this

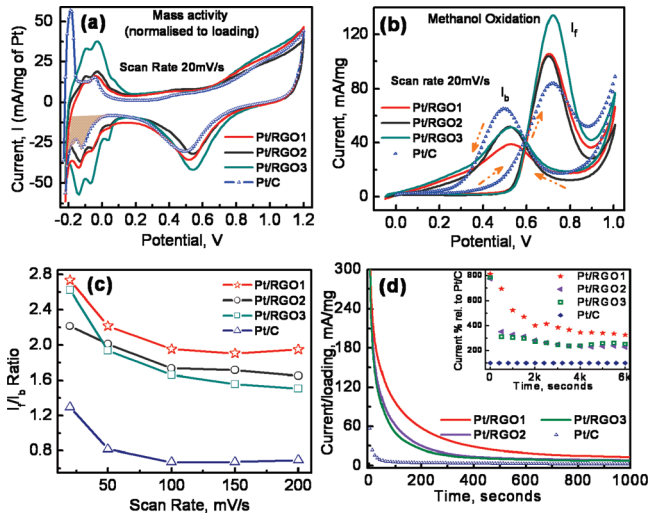

Figure 4. CV responses of Pt/RGO hybrids and Pt/C in N_2-saturated (a) 1 M H_2SO_4 (the shaded region shows the area integrated for hydrogen adsorption) and (b) (1 M H_2SO_4 + 4 M CH_3OH) aqueous solution. *Y*-axis: the electrocatalytic current is normalized to Pt-loading. (c) Scan-rate dependence of I_f/I_b ratio. (d) CA responses of all samples at their respective Vp (Figure 2e) in N_2-saturated (1 M H_2SO_4 + 4 M CH_3OH) solution. Inset: corresponding current−change (%) relative to Pt/C versus time.

reason, we employed TGA measurements (see Supporting Information) performed by using the same samples in powder form, to estimate the metal loading accurately.

Electrochemically Active Surface Area (ECSA). The electrochemically active surface area (ECSA) determines the number of catalytically active sites available for an electrochemical reaction and at the same time accounts for the conductive path available to transfer electrons to and from the electrode surface. However, the catalytic activity of Pt, determined by the interplay of surface, geometric, and electronic factors, is not quite straightforward.

Figure 4a presents the CVs of Pt/RGO hybrids together with Pt/C, deposited on top of a GCE, performed in a N_2-saturated solution of 1 M H_2SO_4 at a potential scan rate of 20 mVs^{-1}. The electrocatalytic current has been normalized to Pt-loading. The well delineated chemical adsorption and desorption peaks of hydrogen on different low-index planes of Pt on RGO became less defined on Pt/C. The ECSA values were calculated on the basis of the hydrogen adsorption charge ($Q_{H\text{-adsorption}}$) in the negative-going potential scan (0 to −0.2 V vs Ag/AgCl) on CVs shown in Figure 4a after correction for double-layer charging (by subtracting the current at 0.2 V from the total current).[23,24]

The ECSAs of Pt/RGO1−3 and Pt/C electrodes were determined to be 43.1, 38.0, 55.5, and 23.7 m^2/g, respectively, and follow the trend Pt/RGO3 > Pt/RGO1 > Pt/RGO2 > Pt/C. The Pt/RGO hybrids exhibited ECSA values 1.6−2.3 times larger than those for Pt/C, with the Pt/RGO3 possessing the largest one. The 134% enhancement in ECSA for Pt/RGO, compared to Pt/C, not only is consistent with the expected effectiveness of a 2D support such as RGO in dispersing Pt NPs but also implies the ease of charge transfer at the Pt-reduced GO interface. It should be mentioned that, despite the presence of significant amount of topological oxygen defects in GO, the long-range crystalline order is maintained.[25,26] This is clear from the selected area electron diffraction (SAED) pattern of GO (Figure S2 in the Supporting Information) that shows the presence of bright spots corresponding to the superposition of two hexagonal lattices from a triple layer GO sheet. Thus, after the reduction process, a higher-order (more graphitised) graphene with enhanced electron-transfer capability is produced.

The concentration of Pt in its metallic state (Pt^0) has been associated with enhanced MOR and electrochemical activity.[27−29] As determined from XPS analysis presented in Figure 3 and table S1 in the Supporting Information, the Pt^0 percentages are 37.8, 27.8, 40.1, and 43.9 for Pt/RGO1, Pt/RGO2, Pt/RGO3, and Pt/C, respectively. The relatively low Pt^0 percentage for Pt/RGO2 is related to the longer microwave exposure time (100 s compared to 50 s for the Pt/RGO1,3), which may lead to increased oxidation of Pt nanocrystals. In order to correlate the ESCA values with the percentage of Pt metallic state in each sample, one should take into account the concentration of Pt on each electrode as indicated in the first column of Table 3. This translates to electroactive Pt^0 concentrations of 1.2 (Pt/RGO1), 1.3 (Pt/RGO2), and 2.7 $\mu g/cm^2$ (Pt/RGO3) and 0.9 $\mu g/cm^2$ (Pt/C) for each electrode, following the trend Pt/RGO3 > Pt/RGO1 ≈ Pt/RGO2 > Pt/C. The trend of Pt^0 concentration agrees well with the trend of ESCA, confirming that the chemical state of Pt is an important factor on determining the electrochemical activity.

In contrast to Pt/C electrode, all three Pt/GO samples have sufficient oxygen content, which helps improve the wettability and accessibility of methanol to the electroactive surface. All three reduced GO supports display sufficient conductivity and interaction with Pt catalysts for facilitating charge transport. Overall, the Pt metal nanocatalyst is the major contributor that determines the ECSA value, whereas the surface oxygen groups play a secondary role on the electrocatalytic activity by modifying the physicochemical properties of the electrode support and allowing efficient electron transfer. It is worth mentioning that, although RGO possesses a substantial amount of oxygen, its conductivity is substantially increased compared to that of GO, permitting efficient charge transfer.

Methanol Oxidation Reaction. The electrocatalytic properties of Pt/RGO hybrids toward the MOR were tested and compared with that of Pt/C. To investigate the electrocatalytic activity of the hybrids, room-temperature CV measurements of the MOR were carried out in N_2-saturated H_2SO_4 (1 M)+CH_3OH (4 M) aqueous solution at a potential scan rate of 20 mVs^{-1} (Figure 4b). The Faradaic current exhibited the well known dependence on the carbon-supported Pt catalyst. The forward anodic peak, around 0.7 V versus Ag/AgCl, is due to the oxidation of methanol and is designated here as I_f. In the backward scan, the oxidation peak at ∼0.5 V versus Ag/AgCl is attributed to the oxidation of CO_{ads}-like species, generated via incomplete oxidation of methanol during the forward scan. This maximum backward peak mass current density is designated as I_b. The I_f value relates directly to the MOR activity of the sample. For the Pt/C system, the forward anodic peak current density of methanol oxidation, I_f (see table 3), is up to 63.5% lower than that of Pt/RGOs, revealing an enhanced methanol oxidation activity for all three Pt/RGO samples. The I_f values follow the same trend as those for ECSA with Pt/RGO3 > Pt/RGO1 > Pt/RGO2 > Pt/C.

Mass Activity. A linear dependence of I_f on the square root of the scan rate could be observed for all samples, confirming that the electrocatalytic oxidation of methanol at the Pt/RGO electrode is controlled by a semi-infinite linear diffusion process (Figure S5 in the Supporting Information). From the magnitude of I_f, it can be seen that the mass activity of Pt/RGO hybrids is considerably higher than that of Pt/C, with Pt/RGO3 showing a value almost 1.6 times higher, which is in perfect agreement with its higher ECSA value (Table 3).

TABLE 3: Compiled Study Comparing CV and CA Results for all the Samples[a]

		CV at 20 mV/s			CA at Vp	
sample	ECSA m^2/g	I_f mA/mg	I_f/I_b	Vp volts	T (s) 10%	I_R % after 300 s
Pt/RGO1 3.08 $\mu g/cm^2$	43.12	105.7	2.73	0.70	132	4.84 (38.87 mA/mg)
Pt/RGO2 4.7 $\mu g/cm^2$	37.99	104.1	2.21	0.69	80	2.52 (18.41 mA/mg)
Pt/RGO3 6.7 $\mu g/cm^2$	55.465	134.0	2.62	0.72	75	2.34 (15.39 mA/mg)
Pt/C 2 $\mu g/cm^2$	23.72	83.9	1.30	0.68	4	0.99 (3.87 mA/mg)

[a] Vp, peak potential; T, time to reach 10% current; I_R %, residual current after 300 s.

CO-Poisoning Tolerance. A large I_f/I_b ratio represents a more complete MOR, less accumulation of CO_{ads}-like species on the catalyst surface, and thus a better CO-poisoning tolerance of Pt catalysts. Consequently, the I_f/I_b is generally used to evaluate the poison tolerance of Pt catalysts. The I_f/I_b ratios of all three Pt/RGO, ranging from 2.73 to 2.6, exhibited a large difference compared with the value of 1.3 of Pt/C. The observation of ~110% enhancement on I_f/I_b values of Pt/RGOs, compared to that of Pt/C, indicates a better CO-poisoning tolerance for all Pt/RGO hybrids. As will be explained in more detail in the following sections, this result demonstrates the beneficial effect of residual oxygen groups on RGO support on reducing the CO-poisoning activity, provided that the catalysts and support are in immediate contact. Further supporting evidence is given when one looks in more detail on the behavior of Pt/RGO samples. Interestingly, Pt/RGO3, although it exhibits the highest ECSA and I_f among all samples, displays a lower I_f/I_b ratio than Pt/RGO1. The superior CO tolerance in Pt/RGO1 is attributed to the increased amount of oxygen groups as well as to the strong interaction between the Pt NPs and the RGO support. On Pt/RGO3, some of the Pt NPs are not in immediate contact with the RGO support as revealed by TEM observations, thus not allowing the beneficial effects of the support on antipoisoning activity to take place.

Figure 4c presents the I_f/I_b ratios as a function of the scan rate. It is clear that the I_f/I_b ratios of all the electrodes decrease initially with increasing scan rate, followed by a more stable behavior after 100 mV/s. It is well known that CO accumulation increases with an increase in scan rate.[30] However, Figure 4c clearly depicts that, irrespective of the scan rate, all three Pt/RGO hybrids exhibit much higher I_f/I_b ratios than the Pt/C, highlighting their strongly reduced poisoning and hence improved stability. For example, Pt/RGO1 showed ~180% enhancement at 200 mV/s compared to Pt/C. A consistent trend of the I_f/I_b ratio with Pt/GO1 > Pt/GO2 > Pt/GO3 ≫ Pt/C is followed at all scan rates with the only exception at 20 mV/s. This slight variation at 20 mV/s could be attributed to the fact that Pt/RGO3 has not reached a stable behavior at this slow scan rate. The lower stability of Pt/RGO3, compared to the other two Pt/RGO electrodes, is further confirmed by results described in the CA studies Section. (Please also check Figure S6 in the Supporting Information, where Figure 5a is replotted for a series of scan rates from 20 to 200 mV/s). It is clear that, at all scan rates, the three Pt/RGO hybrids exhibit the same general trend, displaying much higher I_f/I_b ratios compared to Pt/C, indicating superior antipoisoning behavior. The only slight exception is at the scan rate of 20 mV/s, where the Pt/GO3 showed better I_f/I_b ratio, similar to that observed in Figure 4c. Nevertheless, it is clear that the behavior is consistent, showing systematic and consistent trends, with the proposed mechanism on the role of residual oxygen groups, in particular when the performance of Pt/RGO hybrids is compared with that of commercial Pt/C electrode.

Role of Oxygen Functional Groups. The remarkably strong antipoisoning activity of the Pt/RGO electrocatalysts has been found to be associated with the type and surface density of covalently bound oxygen containing groups remained on the RGO support. The presence of residual oxygen groups on the graphene support can promote the oxidation of CO adsorbed, CO_{ads}, on the active Pt sites via the bifunctional mechanism.[10−12,16] The proposed mechanism is described in the following equations and denoted as 1 in the schematic of Figure 5b:

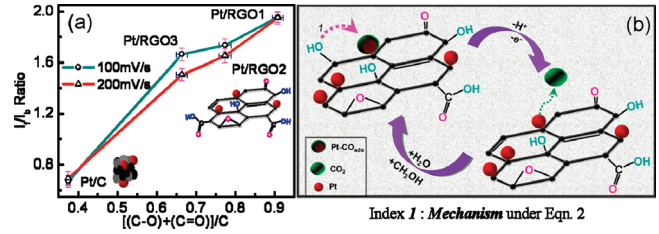

Figure 5. (a) Dependence of I_f/I_b ratio on contribution of residual oxygen species. the X-axis represents the total area under (C−O) + (C═O) deconvoluted peaks divided by the area under whole C1s peak; (C−O) denotes oxygen bonded to carbon by single bond and includes C−OH (hydroxyl) and C−O−C (epoxy, ether), whereas (C═O) denotes oxygen bonded to carbon by double bond and includes >C═O (carbonyl, ketone) and OH−C═O (carboxylic) groups.; (b) Schematic diagram explaining the conversion of adsorbed CO_{ads} species to CO_2 on Pt/RGO hybrids. Index 1 represents the suggested mechanism, facilitated by the presence of residual O-moieties in close proximity to Pt catalyst.

$$RGO + H_2O \rightarrow RGO{-}(OH)_{ads} + H^+ + e^- \quad \text{Forward Scan} \quad (1)$$

$$Pt\text{-}CO_{ads} + RGO{-}(OH)_{ads} \rightarrow CO_2 + H^+ + Pt + RGO + e^- \quad \text{Reverse Scan} \quad (2)$$

Dissociative adsorption of water molecules on the RGO support creates RGO−$(OH)_{ads}$ surface groups adjacent to Pt NPs (eq 1), which readily oxidize CO_{ads} groups on the peripheral Pt atoms (eq 2). The hydrophilic nature of RGO promotes water activation and is the major driver in this mechanism.

In contrast, for Pt/C, with scarcity of oxygen groups, the oxidation of CO_{ads} is known to follow the less efficient Langmuir−Hinshelwood (LH) mechanism.[9,11] The lower efficiency is associated with the high overpotential required for the formation of oxygen-containing species (mainly OH) by water activation on the Pt surface. However, it is obvious that, for the Pt/RGO system, the mechanism described by eqs 1 and 2 would dominate over the LH mechanism, being facilitated by the close proximity of abundant O-moieties and Pt catalysts.

Figure 5a supports the above-mentioned hypothesis, showing a linear dependence of I_f/I_b ratio on the residual O-moieties concentration. All three graphene electrodes, prepared from GO as a starting material, contain residual oxygen groups and exhibit greater catalytic activity for MOR than those from nonoxidized carbon black. Pt/RGO1 with maximum concentration of oxygen

species displayed the best antipoisoning behavior. The oxygen defect sites can be active sites for OH adsorption, thus promoting the oxidation of CO_{ads}. Hence, the oxygen defect sites play a major role in removing the carbonaceous species and contribute to the low catalyst poisoning on the Pt/RGO hybrids, in a way similar to that found in Pt/RuO_2 and $Pt/Ru/MoO_x$ systems.[14,31,32]

Figure S6 in the Supporting Information presents the same dependence as that presented in Figure 5a for a complete series of scan rates ranging from 20 to 200 mV/s. It is clear that, at all scan rates (Figure S6 in the Supporting Information), the three Pt/RGOs exhibit the same general trend electrodes, displaying much higher I_f/I_b ratios compared to that of Pt/C, indicating superior antipoisoning behavior. The only slight exception is at the scan rate of 20 mV/s, where the Pt/GO3 showed better I_f/I_b ratio, similar to that observed in Figure 4c. Nevertheless, it is clear that the behavior is consistent, showing systematic trends verifying the role of residual oxygen groups on the CO tolerance, in particular when the performance of Pt/RGO hybrids is compared with that of commercial Pt/C electrode.

First, the electronic interactions between the oxygen atoms on the graphene and the Pt at the metal/RGO-support interface could also play a role on decreasing the adsorption of CO on Pt. Second, the electron transfer between the oxygen atoms and Pt NPs could lead to enhanced electron density of the latter via a ligand effect.[15,16] Third, at low electrode potentials, hydrogen spillover from the platinum sites to the neighboring RGO facilitates the formation of RGO−(OH) groups. The OH species of RGO can migrate and promote the oxidation of CO_{ads} on the adjacent Pt surfaces. Hydrogen spillover has been suggested as the primary reason for the improved CO tolerance of Pt−Ru−Ni/C nanocomposite as well as for the catalytic oxidation of CO at Pt/WO3 and PtRu/WO3 systems.[33,34] In addition, the higher concentration of oxidized groups on the surface of RGO could facilitate the accessibility of methanol to the electroactive surface.

Although many of the suggested mechanisms for removal of carboneous species are encountered in Pt/metal oxides, the behavior of the two systems (Pt/RGO and Pt/Metal oxide) can differ substantially because the exact nature of the support influences the antipoisoning and catalytic activity of the metal particles by impacting on their morphology (dispersion and degree of agglomeration), adhesion, and electronic structure and by promoting processes such as spillover of oxygen species at the support metal interface.

Chrono-amperometric Studies. Because durability is one of the major concerns in current fuel-cell technology, the stability of Pt/RGO hybrids was further tested by CA measurements at the corresponding forward peak potentials (07−0.8 V) for 1000 s in N_2-saturated 1 M H_2SO_4 solution containing a high methanol concentration of 4 M (Figure 4d). It should be noted that the Pt/RGO hybrids exhibited a much higher initial current compared to Pt/C because of the presence of a larger number of catalytic active sites available for MOR (exemplified by higher ESCA). All electrodes displayed an initial fast current decay followed by a slower attenuation upon long-time operation, reaching a quasi-equilibrium steady state. The initial fast decay is attributed to the formation of intermediate species such as CO_{ads}, CH_3OH_{ads}, and CHO_{ads} during the MOR. The slow attenuation at longer times is due to the adsorption of SO^{-4} anions on the surface of the catalysts. The current decay rates followed the order Pt/RGO1 > Pt/RGO2 > Pt/RGO3 > Pt/C, as illustrated in Table 3. After 300 s of polarization, the Pt/RGO still exhibited current densities one-order higher than those of Pt/C. Pt/RGO1 maintained the lowest current decay rate and the highest current density, approximately 400 times higher than that of Pt/C even after 6K seconds (inset, Figure 4d). The lower stability of Pt/RGO3 can be attributed partly to the heavy Pt loading, with some of the Pt NPs not directly anchored to the O-moieties on RGO support, and thereby suffers from more CO_{ads} accumulation. It is worth mentioning that CA studies for methanol fuel cells are usually performed under mild conditions by employing the onset potential[35] and a relatively low concentration of methanol (1 M). Here, our CA studies were conducted at forward peak potentials and a high concentration of methanol of 4 M, subjecting the hybrids to much harsher conditions. The current response of the commercial Pt/C electrode dropped to 10% of its initial value within 4 s as opposed to the 132 s taken by Pt/RGO1 under the harsh experimental conditions. The long-term stability of Pt/RGO is consistent with the view that the high concentration of residual O-moieties provides OH sites and therefore accelerates the rate of CO_{ads} oxidation.

Conclusion

In summary, we have demonstrated the fabrication of RGO supported Pt NPs electrocatalysts by a simple, environmentally friendly, one-pot microwave-assisted approach. This method has the advantage of making uniformly dispersed NPs, because the significant number of oxygen defects prevents particle agglomeration, which is often a considerable challenge in NP synthesis.

The resulting hybrid material Pt/RGO shows excellent electrocatalytic activity and CO-poisoning tolerance for MOR, outperforming the commercial Pt/C electrocatalysts. We have found that the poisoning ratio I_f/I_b of all Pt/RGO hybrid electrodes is consistently higher than that of the state-of-the-art commercial Pt/C catalysts, which do not possess oxygen on the carbon/Pt interface. Our experimental observations have manifested that the presence of residual oxygen groups on RGO plays a vital role on the removal of carbonaceous species from the adjacent Pt sites. This is implemented through three possible mechanisms. First, the hydrophilic nature of RGO promotes water activation, and as a result, the adsorbed OH species at the platinum edge promote the oxidation of CO. A second possible mechanism is based on the strong interaction between Pt and RGO, which can induce some modulation in the electronic structure of Pt clusters, lowering the Pt−CO binding energy and thus reducing the CO adsorption on Pt. Third, RGO could promote processes such as hydrogen spillover from the Pt catalyst to the RGO support and back spillover of the created hydroxyl species (−OH) from RGO to the adjacent Pt NPs.

The RGO has the obvious additional advantages as a material for catalyst support in fuel-cell technologies including a high (2D) surface area, good accessibility of fuel to the catalyst, and appropriate conductivity despite the presence of residual oxygen groups.

This new hybrid electrocatalyst can be considered as a promising alternative for improving durability of DMFCs and eliminate the use of costly bimetallic or ternary metal systems. Furthermore, our one-pot approach can provide an easy, fast, and eco-friendly way to explore the synthesis of other NPs on RGO, which can be exploited for use in fuel-cell technologies and sensing applications.

Acknowledgment. The work was supported by The Leverhulme Trust (fellowship for A.G., 1-212-R-0197), The Royal Academy of Engineering. EPSRC funded facility access to

HRTEM at University of Oxford University (EP/F01919X/1) and NCESS XPS facility (EP/E025722/1) in Daresbury. Assistance from Dr. D. S. Law and Dr G. Beamson at NCESS and Dr T. Lim at HRTEM facility in Oxford University is acknowledged.

Supporting Information Available: Details of TGA analysis, TEM images of all hybrid samples, high-resolution XPS of Pt/C, and detailed table showing percentage and positions of components as obtained after XPS deconvolutions. The material is available free of charge via the Internet at http://pubs.acs.org.

References and Notes

(1) Czerw, R.; Guo, Z.; Ajayan, P. M.; Sun, Y. P.; Carroll, D. L. *Nano Lett.* **2001**, *1*, 423–427.
(2) Stankovich, S.; Dikin, D. A.; Dommett, G. H. B.; Kohlhaas, K. M.; Zimney, E. J.; Stach, E. A.; Piner, R. D.; Nguyen, S. B. T.; Ruoff, R. S. *Nature* **2006**, *442*, 282–286.
(3) Wen, Z.; Li, J. *J. Mater. Chem.* **2009**, *19*, 8707–8713.
(4) Su, D. S.; Schlögl, R. *ChemSusChem* **2010**, *3*, 136–168.
(5) Rao, C. N. R.; Sood, A. K.; Subrahmanyam, K. S.; Govindaraj, A. *Angew. Chem., Int. Ed.* **2009**, *48*, 7752–7777.
(6) Mu, Y.; Liang, H.; Hu, J.; Jiang, L.; Wan, L. *J. Phys. Chem. B* **2005**, *109*, 22212–22216.
(7) Housmans, T. H. M.; Wonders, A. H.; Koper, M. T. M. *J. Phys. Chem. B* **2006**, *110*, 10021–10031.
(8) Herrero, E.; Franaszczuk, K.; Wieckowski, A. *J. Phys. Chem.* **1994**, *98*, 5074–5083.
(9) Lee, S. W.; Chen, S.; Sheng, W.; Yabuuchi, N.; Kim, Y. T.; Mitani, T.; Vescovo, E.; Shao-Horn, Y. *J. Am. Chem. Soc.* **2009**, *131*, 15669–15677.
(10) Kua, J.; Goddard, W. A., III. *J. Am. Chem. Soc.* **1999**, *121*, 10928–10941.
(11) Liu, Z.; Ling, X. Y.; Su, X.; Lee, J. Y. *J. Phys. Chem. B* **2004**, *108*, 8234–8240.
(12) Li, L.; Xing, Y. *J. Phys. Chem. C* **2007**, *111*, 2803–2808.
(13) Xu, C.; Wang, L.; Wang, R.; Wang, K.; Zhang, Y.; Tian, F.; Ding, Y. *Adv. Mater.* **2009**, *21*, 2165–2169.
(14) Wang, Z. B.; Zuo, P. J.; Yin, G. P. *Fuel Cells* **2009**, *9*, 106–113.
(15) Haner, A. N.; Ross, P. N. *J. Phys. Chem.* **1991**, *95*, 3740–3746.
(16) Park, K. W.; Choi, J. H.; Kwon, B. K.; Lee, S. A.; Sung, Y. E.; Ha, H. Y.; Hong, S. A.; Kim, H.; Wieckowski, A. *J. Phys. Chem. B* **2002**, *106*, 1869–1877.
(17) Li, X.; Chen, W. X.; Zhao, J.; Xing, W.; Xu, Z. D. *Carbon* **2005**, *43*, 2168–2174.
(18) Sieben, J. M.; Duarte, M. M. E.; Mayer, C. E. *ChemCatChem* **2009**, *2*, 182–189.
(19) Muszynski, R.; Seger, B.; Kamat, P. V. *J. Phys. Chem. C* **2008**, *112*, 5263–5266.
(20) Xu, C.; Wang, X.; Zhu, J. *J. Phys. Chem. C* **2008**, *112*, 19841–19845.
(21) Eda, G.; Fanchini, G.; Chhowalla, M. *Nature Nanotechnol.* **2008**, *3*, 270–274.
(22) Dreyer, D. R.; Park, S.; Bielawski, C. W.; Ruoff, R. S. *Chem. Soc. Rev.* **2010**, *39*, 228–240.
(23) Seger, B.; Kamat, P. V. *J. Phys. Chem. C* **2009**, *113*, 7990–7995.
(24) Garsany, Y.; Baturina, O. A.; Lyons, K. E. S.; Kocha, S. S. *Anal. Chem.* **2010**, *82*, 6321–6328.
(25) Lerf, A.; He, H.; Forster, M.; Klinowski, J. *J. Phys. Chem. B* **1998**, *102*, 4477–4482.
(26) Jeong, H. K.; Lee, Y. P.; Lahaye, R. J.; Park, M. H.; An, K. H.; Kim, I. J.; Yang, C. W.; Park, C. Y.; Ruoff, R. S.; Lee, Y. H. *J. Am. Chem. Soc.* **2008**, *130*, 1362–1366.
(27) Liu, S. H.; Yu, W. Y.; Chen, C. H.; Lo, A. Y.; Hwang, B. J.; Chien, S. H.; Liu, S. B. *Chem. Mater.* **2008**, *20*, 1622–1628.
(28) Park, K. W.; Han, D. S.; Sung, Y. E. *J. Power Sources* **2006**, *163*, 82–86.
(29) Prabhuram, J.; Zhao, T. S.; Wong, C. W.; Guo, J. W. *J. Power Sources* **2004**, *134*, 1–6.
(30) Koper, M. T. M.; Lukkien, J. J.; Jansen, A. P. J.; van Santen, R. A. *J. Phys. Chem. B* **1999**, *103*, 5522–5529.
(31) Cao, L.; Scheiba, F.; Roth, C.; Schweiger, F.; Cremers, C.; Stimming, U.; Fuess, H.; Chen, L.; Zhu, W.; Qiu, X. *Angew. Chem., Int. Ed.* **2006**, *45*, 5315–5319.
(32) Rolison, D. R.; Hagans, P. L.; Swider, K. E.; Long, J. W. *Langmuir* **1999**, *15*, 774–779.
(33) Liang, Y.; Zhang, H.; Tian, Z.; Zhu, X.; Wang, X.; Yi, B. *J. Phys. Chem. B* **2006**, *110*, 7828–7834.
(34) Micoud, F.; Maillard, F.; Bonnefont, A.; Jobc, N.; Chateneta, M. *Phys. Chem. Chem. Phys.* **2010**, *12*, 1182–1193.
(35) Lin, M. L.; Lo, M. Y.; Mou, C. Y. *J. Phys. Chem. C* **2009**, *113*, 16158–16168.

JP107872Z